



Article

Pt-Embedded Metal-Organic Frameworks Deriving Pt/ZnO-In₂O₃ Electrospun Hollow Nanofibers for Enhanced Formaldehyde Gas Sensing

Lei Zhu ^{1,2}, Ze Wang ¹, Jianan Wang ^{1,*}, Jianwei Liu ^{1,3}, Jiaxin Zhang ¹ and Wei Yan ^{1,*}

- Xi'an Key Laboratory of Solid Waste Resource Regeneration and Recycling, State Key Laboratory of Multiphase Flow Engineering, School of Energy and Power Engineering, Xi'an Jiaotong University, Xi'an 710049, China; leizhu@xjtu.edu.cn (L.Z.)
- School of Physics and Electrical Engineering, Weinan Normal University, Chaoyang Street, Weinan 714099, China
- ³ School of Chemistry and Chemical Engineering, Xi'an University of Science & Technology, Xi'an 710054, China
- * Correspondence: wangjn116@xjtu.edu.cn (J.W.); yanwei@xjtu.edu.cn (W.Y.)

Abstract: Functionalization by noble metal catalysts and the construction of heterojunctions are two effective methods to enhance the gas sensing performance of metal oxide-based sensors. In this work, we adopt the porous ZIF-8 as a catalyst substrate to encapsulate the ultra-small Pt nanoparticles. The Pt/ZnO-In₂O₃ hollow nanofibers derived from Pt/ZIF-8 were prepared by a facile electrospinning method. The 25PtZI HNFs sensor possessed a response value of 48.3 to 100 ppm HCHO, 2.7 times higher than the pristine In₂O₃, along with rapid response/recovery time (5/22 s), and lower theoretical detection limit (74.6 ppb). The improved sensing properties can be attributed to the synergistic effects of electron sensitization effects and catalytic effects of Pt nanoparticles, and the high surface O^- absorbing capability of heterojunctions. The present study paves a new way to design high performance formaldehyde gas sensors in practical application.

Keywords: HCHO sensing; Pt nanoparticles; MOFs; heterojunctions; nanofibers



Citation: Zhu, L.; Wang, Z.; Wang, J.; Liu, J.; Zhang, J.; Yan, W. Pt-Embedded Metal–Organic Frameworks Deriving Pt/ZnO-In₂O₃ Electrospun Hollow Nanofibers for Enhanced Formaldehyde Gas Sensing. Chemosensors 2024, 12, 93. https://doi.org/10.3390/ chemosensors12060093

Received: 24 April 2024 Revised: 24 May 2024 Accepted: 29 May 2024 Published: 31 May 2024



Copyright: © 2024 by the authors. Licensee MDPI, Basel, Switzerland. This article is an open access article distributed under the terms and conditions of the Creative Commons Attribution (CC BY) license (https://creativecommons.org/licenses/by/4.0/).

1. Introduction

Formaldehyde (HCHO) is one of the common toxic substances in indoor air pollution, widely found in decorative materials used in newly renovated houses, building materials, and furniture [1–3]. High indoor HCHO concentration can lead to tearing and eye sensitivity. Long-term exposure to even low concentrations of HCHO can pose serious health hazards, such as chronic respiratory diseases and even cancer [4,5]. The World Health Organization (WHO) has established a guideline for formaldehyde levels in indoor air, setting the threshold at 0.1 mg/m³ (80 ppb) [6]. Therefore, effective detection of indoor HCHO pollution is essential to protecting residents' health and safeguarding indoor air quality.

Gas sensors based on metal oxide semiconductors (MOS) (e.g., SnO_2 [7,8], In_2O_3 [9,10], ZnO [11,12], and NiO [13,14]) have attracted great attention for volatile organic compounds detection due to their easy fabrication, simple operation, cost-effectiveness, and real-time monitoring [15]. Among them, In_2O_3 is a significant n-type semiconductor with a wide band gap (3.55–3.75 eV) [16], and high electrical conductivity and stability (thermal and chemical), which has been proven to be an ideal material for gas sensing [17]. Nevertheless, the pure In_2O_3 sensors suffer from low levels of gas sensing response, high operating temperatures (≥ 200 °C), and limited selectivity, ultimately restricting their implementation in practical gas detection.

Elaborate design of noble metal catalysts with high catalytic activity is a feasible way to enhance the sensitivity of the MOS gas sensor [18,19], and reduce the activation energy between the metal oxide and the target gas, thus facilitating the chemical gas sensing

reaction. Zhang et al. [20] proposed Pt nanoparticles (NPs) loaded on a BiVO₄-based sensor for acetone sensing as the response value of Pt-BiVO₄ is higher than that of the BiVO₄ sensor alone due to the synergistic effects of Pt electronic and chemical sensitizations. Zhao et al. [21] synthesized Pd-In₂O₃ for methane detection, and the enhancement in sensing capabilities can be attributed to the incorporation of Pd. Liu et al. [22] prepared Ag-SnO₂ nanoparticles for high sensitivity monitoring of HCHO at a low operating temperature of 125 °C. Nevertheless, the problem of particle aggregation may affect the performance of noble metal catalysts, as such aggregation may obscure the active sites and reduce their catalytic efficacy, ultimately causing catalytic performance degradation. Loading the catalyst onto the substrate is an effective strategy to promote the exposure of the active sites and helps to enhance the catalytic efficiency of the catalyst.

Zeolite Imidazolate Frameworks (ZIFs) have been attracting much attention in the field of chemical sensors due to their extremely high specific surface area, abundant open metal active sites, and tunable structural properties [23,24]. The highly porous nature and ordered pore channel characteristics of ZIFs provide conditions for embedding noble metal NPs. The formation and aggregation processes of noble metal NPs are limited by these pore structures, thus ensuring a high dispersion and uniform distribution of ultra-small noble metal NPs on the surface of ZIFs [25]. Notably, ZIF-8 is one of the most representative ZIF materials with a sizable cavity measuring 11.6 Å and a relatively smaller pore size of 3.4 Å. This material is characterized by the presence of Zn^{2+} ions at the metal center and the use of 2-Methylimidazole (2-MeIm) as the coordinating ligand [26]. These features make it a potential catalyst substrate for enhancing the catalytic efficiency of noble metal NPs, thus facilitating the gas sensing performance.

Herein, we rationally designed and fabricated Pt/metal–organic framework (MOF)-derived Pt/ZnO-In $_2$ O $_3$ electrospun hollow nanofibers (PtZI HNFs) for efficient HCHO gas sensing. The sensing properties of pristine In $_2$ O $_3$ and PtZI HNFs with different amounts of Pt NPs (0.5, 1.0, 2.5, and 5.0 wt%) are comparatively investigated. The sensor based on 25PtZI HNFs shows a response value of 48.3 toward 100 ppm HCHO at 180 °C, 2.7 times higher than that based on the pristine In $_2$ O $_3$ sensor, with a faster response speed (5 s) and lower detection limit (74.6 ppb) for HCHO detection. The improved HCHO sensing mechanism of the 25PtZI HNFs sensor is further explored by analyzing the experimental data.

2. Experimental Section

2.1. Synthesis of ZIF-8 Nanoparticles (NPs)

Typically, 1.2 g Zn $(NO_3)_2 \cdot 6H_2O$ and 2.6 g 2-methylimidazole were added into an 80 mL methanol solution and stirred for 6 h at ambient temperature. After that, the obtained white precipitate was centrifuged and washed three times with methanol. Ultimately, the obtained ZIF-8 crystals were dried in an oven at a temperature of 80 °C for a period of 24 h.

2.2. Synthesis of Pristine Electrospun In_2O_3 Hollow Nanofibers and Pt-Embedded ZIF-8-Derived $Pt/ZnO-In_2O_3$ Electrospun Hollow Nanofibers (PtZI HNFs)

PtZI HNFs were prepared by electrospinning technique and subsequent annealing treatment. Firstly, 0.1 g ZIF-8 was dispersed into 4 mL ethanol with 0.25 mL of 10 mg mL $^{-1}$ H₂PtCl₆·6H₂O solution. Then, NaOH solution containing 0.008 g of NaBH₄ was added dropwise as a reducing agent to reduce Pt⁴⁺ to Pt. The above mixture was sonicated for 30 min to form solution A. Meanwhile, 1 g In(NO₃)₃·4.5H₂O was added into 8 mL N, N-dimethylformamide with stirring for 2 h to form solution B. Then, the above A and B solutions with the addition of 1 g PVP were mixed, and magnetically stirred for another 12 h. The homogeneously mixed solution was transferred into a 10 mL syringe for electrospinning under an electrostatic field strength voltage of ~13 kV. Finally, the precursor fibers were subsequently calcined at a temperature of 600 °C for 3 h in air atmosphere with a heating rate of 5 °C·min $^{-1}$ to form 25PtZI HNFs (the addition of Pt is 0.25 wt%, which is named 25PtZI). In this work, the samples of Pt content were changed to 0.05, 0.10, and 0.5 wt%, which are denoted as 05PtZI, 10PtZI, and 50PtZI HNFs. The pristine In₂O₃

HNFs were synthesized by the same process without the addition of ZIF-8, $H_2PtCl_6 \cdot 6H_2O$, and $NaBH_4$.

2.3. Characterizations

Morphological data and elemental distribution mapping were examined by scanning electron microscope (SEM; GeminiSEM 500, China) and equipped with an energy dispersive spectrometer (EDS) system. Transmission electron microscopy (TEM; JEOL JEM2100, Japan) was conducted to study more detailed morphological data of the samples. X-ray diffraction (XRD) patterns were acquired on a PANalytical X'pert MPDPro (Netherlands) using a Cu Kα radiation source. Fourier-Transform Infrared Spectroscopy (Bruker Tensor 37 spectrometer, China) was used to determine surface functional groups and chemical bonds of samples. An HR800 Raman spectrometer (France) was used for Raman scattering; excitation was carried out with 532 nm laser light. The specific surface area and pore sizes of the samples were detected by N₂ adsorption/desorption using an SSA-4300 (China) instrument. An AXIS ULtrabld (England) instrument was used to obtain X-ray photoelectron spectroscopy (XPS) using a monochromatic Al Kα radiation source (15 kV, 1486.6 eV). Thermogravimetric analysis (TGA) was performed on a TGDTG-60FTIR (China) apparatus with a heating rate of 10 °C min⁻¹ from room temperature to 800 °C under air atmosphere. The composition of the sample was analyzed by an inductively coupled plasma atomic emission spectrometry (ICP-AES-9000, Japan) instrument.

2.4. Gas Sensing Measurements

The performance of the gas sensor was assessed utilizing the WS-30A measurement system. The specific description is shown in Text S1. A static liquid gas distribution method was used to prepare the different concentrations of tested gases. The evaporation system quickly volatilizes a certain volume Q injected liquid into vapor. The volume Q can be obtained by Equation (S1).

3. Result and Discussion

3.1. Microstructures and Composition

The PtZI HNFs were obtained by integrating the chemical precipitation method and electrospinning technique as illustrated in Figure 1. Firstly, uniform ZIF-8 nanocrystals were prepared by a chemical precipitation method. Subsequently, the as-obtained ZIF-8 polyhedrons were dispersed in ethanol with a certain amount of $H_2PtCl_6\cdot 6H_2O$ solution. Benefiting from the skeleton structure of ZIF-8 combined with ultrasonic treatment, the ultra-small Pt NPs restricted within the cavities of ZIF-8 were obtained by the sodium borohydride reduction method. The amount of Pt NPs can be adjusted by adding the amount of $H_2PtCl_6\cdot 6H_2O$ to the reaction system. Then, the ethanol solution containing Pt/ZIF-8 was mixed with a DMF solution containing In³⁺ to yield a homogeneous electrospinning precursor. The Pt/ZIF-8 particles can be encapsulated into the precursor nanofibers by the electrospinning technique. Finally, the Pt-incorporated ZIF-8 nanoparticle-derived Pt/ZnO-In₂O₃ hollow nanofibers were obtained after annealing in air.



Figure 1. Schematic illustration of the synthetic process of Pt/ZIF-8-derived Pt/ZnO-In₂O₃ HNFs.

Chemosensors **2024**, 12, 93 4 of 14

The morphologies of as-prepared pristine In₂O₃, 05PtZI, 10PtZI, 25PtZI, and 50PtZI HNFs were analyzed through the SEM images. Figure 2a-e show that all the samples present a disordered fiber stacking morphology. The pristine In₂O₃ HNFs have a relatively smooth surface with a hollow nanofiber structure (Figure 2a). Due to the evaporation of volatile compounds in Pt/ZIF-8 by high-temperature calcination, the nanofibers modified by Pt/ZIF-8 generated an abundance of pores [27] (Figure 2b-e). The high porosity within the nanofiber offers significant advantages for the functionality of gas sensors, as it allows gas molecules to penetrate deeper into the sensing material more quickly, and offers more adsorption sites for gas molecules. This results in an improved capacity to shorten the sensor's response time and to detect lower concentrations of gases [28–30]. However, with the highest loading amount of Pt, the continuous nanofiber morphology is slightly disrupted as a result of the heightened viscosity within the spinning solution and the internal stress within the fibers, which is caused by the change in the proportion of metal ions relative to the content of PVP [31] (insert of Figure 2e). Therefore, the appropriate amount of Pt loading is very important to maintain the morphology and structure of continuous nanofibers.

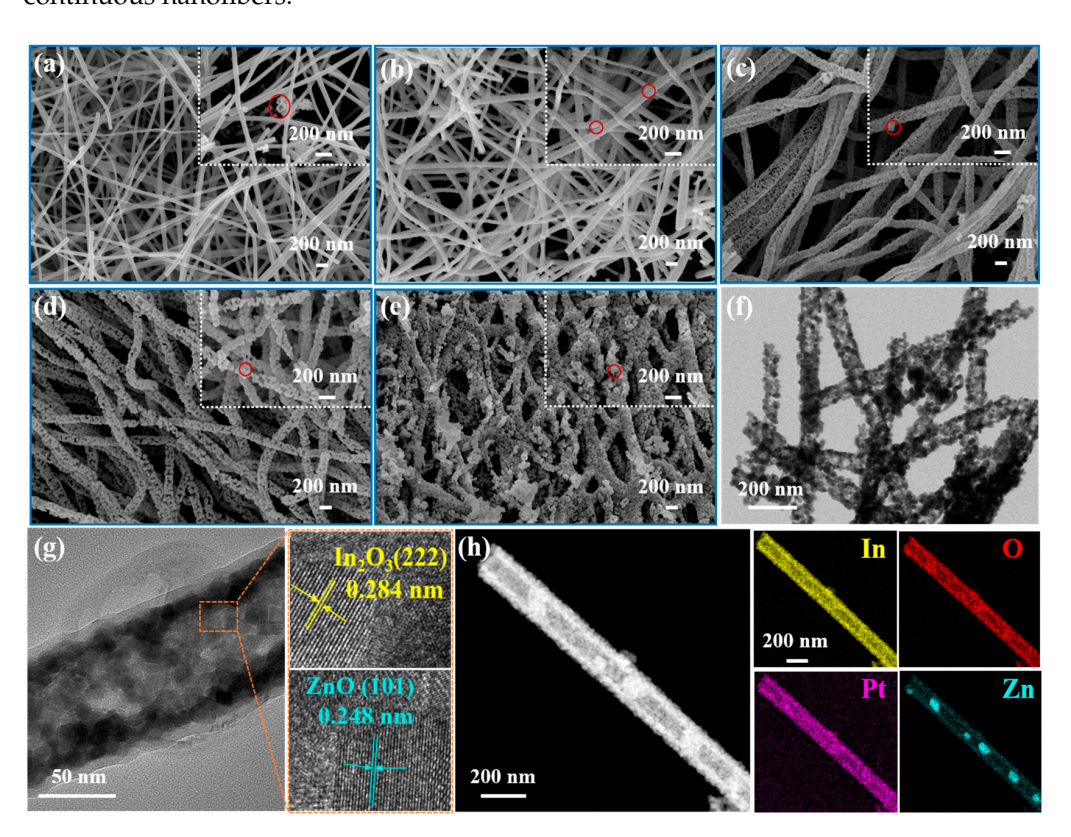


Figure 2. SEM images of (a) pristine In₂O₃, (b) 05PtZI, (c) 10PtZI, (d) 25PtZI, and (e) 50PtZI samples; (f) TEM image, (g) corresponding HRTEM image, and (h) EDS element mapping of 25PtZI HNFs.

Figure 2f presents the TEM image of 25PtZI HNFs under low magnification. As can be seen from the figure, these nanofibers are translucent and consist of sparse nanoparticles, confirming the hollow and porous morphology. According to the high-resolution TEM image in Figure 2g, the crystal planes of In_2O_3 (222) and ZnO (101) have characteristic lattice fringe spacings of 0.284 nm and 0.248 nm, respectively. Accordingly, the nanofibers are composed of In_2O_3 nanoparticles and ZnO nanoparticles, which indicates that the Zn ions from ZIF-8 are converted to ZnO and n-n heterojunctions are formed. Furthermore, the EDS mapping in Figure 2h demonstrates the 25PtZI nanofibers are mainly composed of In, O, Pt, and Zn. Additionally, unlike the evenly distributed elements of In, O, and Pt throughout the nanofibers, the element Zn exhibits a bead-like distribution over the nanofibers. This further confirms the conversion of the polyhedron ZIF-8 into ZnO after

Chemosensors **2024**, 12, 93 5 of 14

annealing treatment. As presented in Figure S1, the EDS spectra show the compositional elements of all samples. In addition, the low concentrations of Zn and Pt compositions of the four PtZI samples were determined by the ICP-AES in Table S1.

XRD patterns of the pristine In_2O_3 , 05PtZI, 10PtZI, 25PtZI, and 50PtZI HNFs were investigated to reflect the crystalline structure as displayed in Figure 3a. The main peaks in all samples show the typical cubic In_2O_3 phase (JCPDS No. 06-0416). For four PtZI samples, there are five shallow peaks at 31.76, 34.42, 36.25, 47.53, and 56.60° consistent with the (100), (002), (101), (102), and (110) planes, respectively, which are characteristic of ZnO (JCPDS No. 36-1451) [7]. In addition, due to the low Pt contents (0.05, and 0.10 wt%), no Pt characteristic peaks were found in the XRD patterns of 05PtZI and 10 PtZI HNF. As the Pt content increased to 0.25 and 0.50 wt%, the peaks of 25PtZI and 50PtZI samples at 39.76, 46.24, and 67.45° confirm the existence of Pt NPs (111), (200), and (220) (JCPDS No. 04-0802) planes [32], respectively.

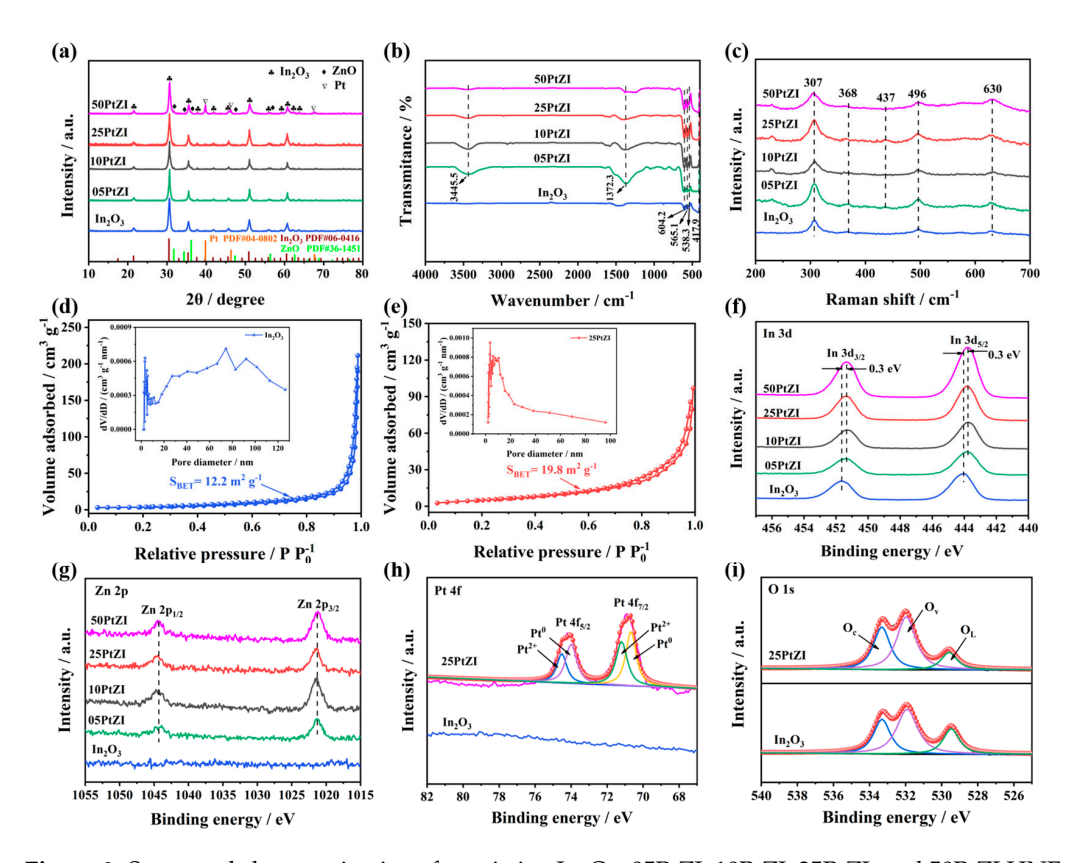


Figure 3. Structural characterizations for pristine In_2O_3 , 05PtZI, 10PtZI, 25PtZI, and 50PtZI HNFs. (a) XRD patterns; (b) FT-IR spectra; (c) Raman spectra of various samples. N_2 adsorption-desorption isotherms and pore-size distributions of (d) pristine In_2O_3 and (e) 25PtZI HNFs; XPS spectra of (f) In 3d, and (g) Zn 2p of all samples; XPS spectra of (h) Pt 4f and (i) O 1s of pristine In_2O_3 and 25Pt HNFs.

To substantiate the synergetic crystalline structure, the FT-IR measurement was employed for the as-synthesized samples. As displayed in Figure 3b, all samples possess four characteristic peaks at 417, 538, 565, and 604 cm⁻¹, corresponding to the In-O bonds of the cubic In₂O₃ phase [33]. For PtZI samples, the appearance of a band around 496 cm⁻¹ attributed to the Zn-O bond confirms the formation of ZnO [34]. The band at 1415 cm⁻¹ corresponds to the mode of CO_3^{2-} [35]. Additionally, a broad absorption peak is present at 3445 cm⁻¹ caused by stretching vibrations of the hydroxyl groups in water (-OH) [36]. Figure 3c presents the Raman spectra of pristine In₂O₃ and various PtZI composites. Four Raman scattering peaks of all samples were observed at 307, 368, 496, and 630 cm⁻¹, which can be assigned to $\delta(InO_6)$, In-O-In, $\nu(InO_6)$, and $\nu(InO_6)$ vibrations of cubic In₂O₃ [37,38],

Chemosensors **2024**, 12, 93 6 of 14

respectively. The new Raman peak at around 437 cm $^{-1}$ can be observed in four PtZI samples, indicating the $E_{2(H)}$ mode of ZnO [39].

The textural properties of the samples were further probed through the technique of nitrogen adsorption—desorption analysis. For pristine In_2O_3 and 25PtZI HNFs, the N_2 adsorption/desorption isotherms depicted in Figure 3d,e exhibit the typical III isotherm pattern accompanied by H3 hysteresis loops, which are indicative of the existence of mesopores [40]. The BET surface areas of pristine In_2O_3 and 25PtZI HNFs are 12.2, and 19.8 m² g⁻¹, respectively. The higher surface area of 25PtZI HNFs demonstrates the enhanced gas adsorption performance. The calculated pore size distribution of pristine In_2O_3 (insert of Figure 3d) displays two maxima at 3.4, and 74.2 nm, attributing to the dimensions of the nanopores and the interstices between adjacent nanofibers, respectively. Moreover, the pore size of 25PtZI HNFs is mainly distributed about 3.6 nm (mesoporous) in the insert of Figure 3e, which is smaller than that of pristine In_2O_3 HNFs. Gas molecules can be adsorbed—desorbed and diffused through these mesopores, resulting in improved sensitivity. Thus, the as-prepared 25PtZI HNFs have high specific surface areas and proper pore size distributions, making them ideal for high-performance gas sensors [41].

The XPS spectra of all samples are obtained for analysis the elemental composition and valence states. In all samples, peaks corresponding to In $3d_{5/2}$ and In $3d_{3/2}$ were found at 444.0–443.7 eV and 451.6–451.3 eV, respectively, demonstrating the presence of In^{3+} (Figure 3f) [23]. In addition, based on the In 3d XPS spectra, binding energies of PtZI samples are lower than those of pristine In₂O₃, suggesting that In electron density is increased on the surface relative to pristine In₂O₃, thereby lowering the binding energies [42]. For Zn 2p spectra (Figure 3g), peaks belonging to Zn $2p_{3/2}$ and Zn $2p_{1/2}$ of Zn²⁺ at 1021.8 eV and 1044.7 eV were observed in four PtZI HNFs, respectively, due to the formation of ZnO [43]. The Pt 4f spectral data presented in Figure 3h exhibit two distinct peaks that are characteristic of the $4f_{7/2}$ and $4f_{5/2}$ electronic states in 25PtZI HNFs. The peaks are assigned to surface decorated Pt⁰ nanoparticles (70.7 and 74.0 eV) alongside partially oxidized surface species P^{t2+} (71.1 and 74.5 eV) [44]. The results demonstrate that a coordination effect exists among Pt, ZnO, and In₂O₃, which implies a strong interaction at the interface of the Pt NPs with the ZnO-In₂O₃ heterojunction [45]. The O 1s spectra of pristine In₂O₃ and 25PtZI HNFs (Figure 3i) were fitted into three peaks located at binding energy of 529.4, 531.9, and 533.3 eV, attributed to the lattice oxygen (O_L), oxygen vacancies (O_V), and chemisorbed oxygen (O_C) on the surface of the samples [45]. The area occupied by different types of oxygen in the O 1s spectrum is used to measure their percentage. The proportions of the three oxygen content types are displayed in Table S2. It is evident that in comparison to pristine In₂O₃, the percentage of O_L in 25PtZI decreased from 21.6 to 13.8%, the percentage of O_V increased from 48.4 to 50.4%, and the percentage of O_C increased from 30.0 to 35.8%. The increase in the level of the concentration of the O_V and O_C can be attributed to the existence of Pt NPs, which interact with adsorbed oxygen, leading to surface defects such as oxygen vacancies on the ZnO-In₂O₃ surface [46]. Results show that 25PtZI HNFs can provide more oxygen adsorption sites as well as absorb more chemisorbed oxygen in surface sensing reactions, contributing to improving sensing performance.

3.2. Gas Sensing Properties

The gas sensing properties of sensors based on pristine In_2O_3 , 05PtZI, 10PtZI, 25PtZI, and 50PtZI HNFs were systematically measured. Operating temperature is a critical determinant in the efficacy of MOS-based gas sensors. It not only provides the energy required for the chemical reaction between gas molecules and the surface of the metal oxide, but also determines how gas molecules are adsorbed and desorbed on the metal oxide surface [47,48]. Specifying the optimum operating temperature is crucial for achieving the best gas sensing properties. The responses of five sensors toward 100 ppm HCHO were evaluated at various temperatures across a range of 120–220 °C (Figure 4a). The results of five sensors indicate that response values trend upward until reaching the maximum of 17.1 (In_2O_3), 21.7 (05PtZI), 26.2 (10PtZI), 48.3 (25PtZI), and 27.2 (50PtZI) at 180 °C.

Then, the responses decreased as the operating temperature increased from 180 to 220 °C. Among them, the 25PtZI-based sensor exhibits the highest response values, 2.7-fold higher than the pristine In₂O₃ sensor. The enhancement in the HCHO response value is due to the synergistic impact of Pt NPs and the n-n heterojunction of ZnO-In₂O₃. However, with the increasing load of Pt NPs, the response value of the 50PtZI sensor to HCHO decreases. This may be because excess Pt NPs lead to agglomeration and the subsequent occupation of a restricted number of active sites on the surface of In₂O₃, thus hindering the interaction between HCHO gas molecules and the adsorbed oxygen and reducing the catalytic activity [46]. Figure S2 shows the plots of resistance versus temperature for all sensors. The results present that the resistance of all sensors undergoes a decrease as the temperature rises, a trend that is related to the enhancement of intrinsic excitation of the MOS at elevated temperatures. Specifically, temperature-excited valence band electrons jump to the conduction band, increasing in the conduction band electron density and thus enhancing conductivity [46,49]. In addition, with the increase of the Pt NPs contents, the baseline resistance at 180 °C for pristine In₂O₃, 05PtZI, 10 PtZI, 25PtZI, and 50 PtZI sensors exhibits a higher trend (Figure S2). The different work functions of In₂O₃, Pt, and ZnO provide the driver for the electron transfer in the interface. When In₂O₃, Pt, and ZnO combine, electrons flow from In₂O₃ to Pt and ZnO, resulting in a thicker electron depletion layer at their interface. The increase of electronic depletion layer thickness results in the increase of baseline resistance in air [50,51].

Figure 4b and Figure S3 depict the response–recovery curves of all sensors when exposed to a concentration of 100 ppm HCHO at 180 °C. Upon exposure to the HCHO atmosphere, the resistance of sensors will rapidly decrease to a stable low-resistance state. When sensors are returned to the air atmosphere, the resistance increases to its initial stabilized value (Figure 4b). The response/recovery times of sensors based on pristine In₂O₃, 05PtZI, 10PtZI, 25PtZI, and 50PtZI are 7/31 s, 5/14 s, 5/9 s, 5/22 s, and 6/16 s, respectively. It is evident that the modification by Pt/ZIF-8 nanocage-derived Pt/ZnO substantially enhances both the response and recovery rates compared to pristine In₂O₃. The accelerated response recovery rates of various PtZI sensors can be ascribed to the exceptional catalytic capabilities of Pt NPs, which can rapidly dissociate a large number of oxygen molecules to form adsorbed oxygen ions, thus accelerating the surface redox process [52].

Furthermore, the selectivity capacity of the five sensors have been examined toward different gases (100 ppm) at 180 °C (Figure 4c). The 25PtZI sensor exhibited a significantly greater response to HCHO compared to other interfering gases. Specifically, the 25PtZI sensor's response to HCHO was 5.8 times higher than that to ethanol and 40 times higher in comparison to toluene and benzene. Meanwhile, the response value of 25PtZI sensor toward HCHO is the highest among all sensors, demonstrating its outstanding selectivity. The low bond dissociation energy of HCHO (364 kJ/mol) may explain its high selectivity over other interference gases, which was easier to break.

Figure 4d shows the dynamic response of all sensors exposed to different concentrations of HCHO. As the concentration of HCHO rose from 0.5 to 100 ppm, the responses of the five sensors gradually increased. Specifically, the 25PtZI sensor shows the highest response value compared to the pristine In_2O_3 and other PtZI sensors. Additionally, the response of 25PtZI sensor is 2.8 toward HCHO concentration as low as 500 ppb, which is two times higher compared to the pristine In_2O_3 sensor (1.4) (insert in Figure 4d). This indicates that the enhanced HCHO sensing performance can be achieved by the optimum addition of Pt NPs. The responses of the In_2O_3 and 25PtZI sensors show a direct proportionality to the concentration of HCHO in the range of 500 ppb to 100 ppm, indicating a linear relationship between the two variables (Figure 4e). The limit of the detection (LOD) values is calculated by the Equation (1):

$$LOD = 3 \times RMS_{noise} / slope$$
 (1)

where RMS_{noise} denotes the root mean square noise based on 30 experimental baselines in air. The slope can be obtained in the concentration–response curve. After calculation, the LOD of the 25PtZI sensor to HCHO gas is calculated as low as 74.6 ppb, which is lower than that of the In_2O_3 sensor (163.8 ppb). Moreover, the five-repeated response/recovery curves of the 25PtZI sensor toward 100 ppm HCHO at 180 °C are tested in constant experimental conditions. As shown in Figure 4f, the response value of the 25PtZI sensor only fluctuates slightly with unchanged response/recovery times, suggesting the excellent repeatability of the 25PtZI sensor [11].

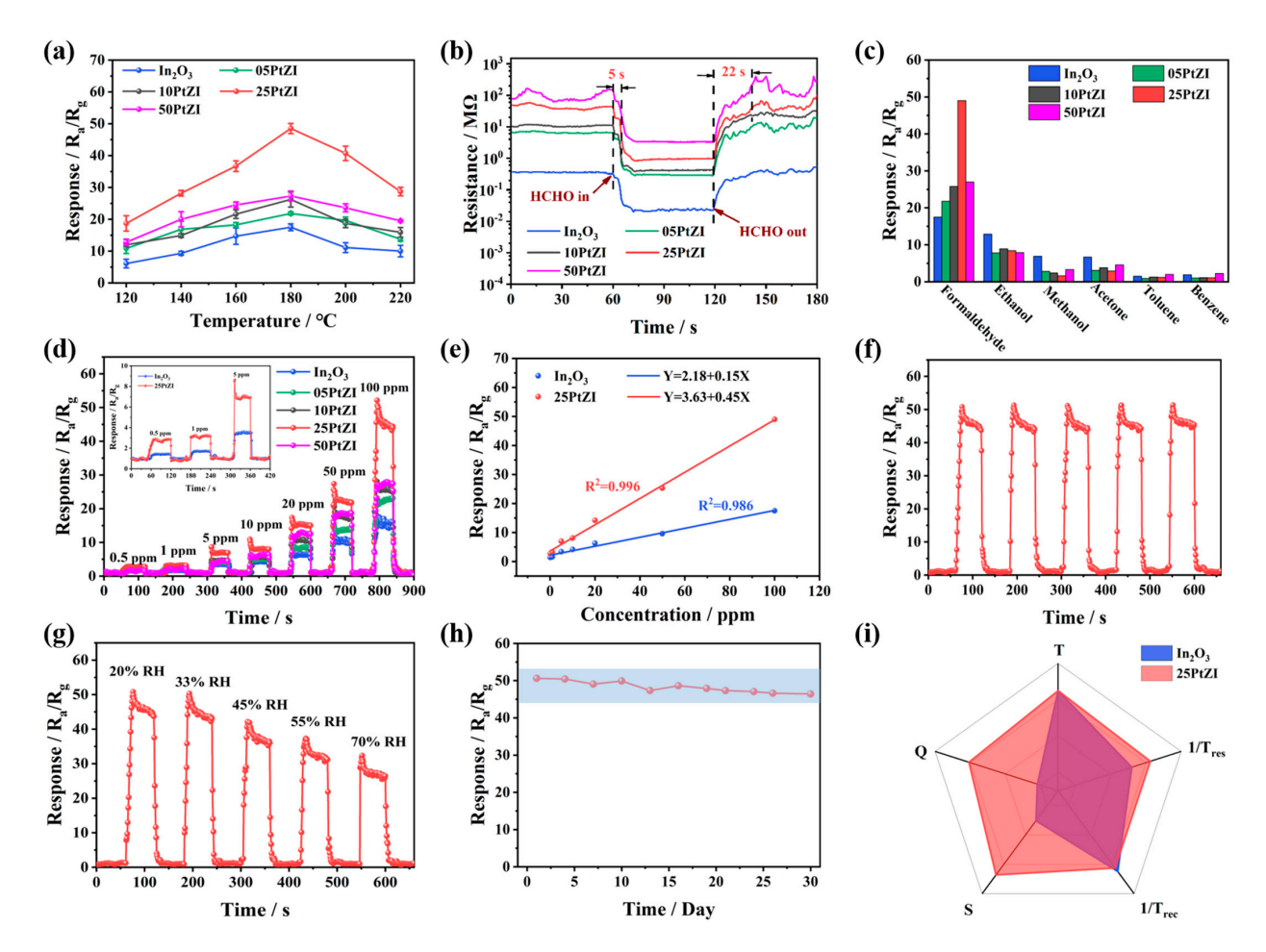


Figure 4. Sensing properties measurements for pristine In_2O_3 , 05PtZI, 10PtZI, 25PtZI, and 50PtZI HNFs sensors at 180 °C. (a) Response toward HCHO (100 ppm) under different operating temperatures; (b) response and recovery characteristics of sensors exposure to HCHO (100 ppm); (c) selectivity of sensors toward 100 ppm of various gas; (d) response curves of sensors to HCHO from 0.5 to 100 ppm concentrations; (e) linearity between the concentration of sensors and the response value; (f) repeatability of the 25PtZI sensor to HCHO (100 ppm); (g) dynamic response curves of the pristine 25PtZI sensors to HCHO (100 ppm) under different relative humidities (RHs); (h) long—term stability of 25PtZI sensor towards HCHO (100 ppm); (i) five-axe spider-web diagram for evaluating the optimal work condition of pristine In_2O_3 and 25PtZI HNFs based sensors.

The interference of humidity on the sensitivity of the pristine In_2O_3 and 25PtZI sensors to 100 ppm HCHO has also been performed in the relative humidity (RH%) range of 20–70 (Figure 4g). The controlled humidity environment in the test chamber is achieved by water evaporation. The response of the 25PtZI sensor toward 100 ppm HCHO progressively diminishes as the relative humidity is increased from 45% to 70%RH. In humid conditions, SMO-based sensors provide a reduced response because oxygen molecules on the surface react with water molecules and occupy active sites, interfering with the adsorption of

HCHO gas molecules [29,53]. As the relative humidity increased to 70%, the 25PtZI sensor still retained approximately 57% of the original response, showing good anti-humidity properties. As presented in Figure 4h, the response of the 25PtZI sensor toward HCHO barely fluctuated over 30 days, implying significant long-term stability of the 25PtZI sensor.

The five-axe spider-web plot of the operating temperature (1/T), response/recovery speed ($1/\tau_{res}$, $1/\tau_{rec}$), response (S), and selectivity (Q) is proposed to determine the optimal work condition of pristine In_2O_3 and 25PtZI sensors, as depicted in Figure 4i. The orange region (25PtZI) in the spider web plot is larger than the blue region (pristine In_2O_3), which indicates that the 25PtZI HNFs sensor can obtain the optimal working conditions as well as the high gas sensing performance [54].

Compared with other semiconductor oxide-based HCHO sensors, the gas-sensing performance is shown in Table S3. The 25PtZI-based sensor in our work presents high response as well as rapid response speed at a relatively lower operating temperature.

3.3. Gas Sensing Mechanism

In this work, a conventional chemisorption-based oxygen-related resistive modulation model systematically accounts for the sensitization mechanisms of 25PtZI HNFs (Figure 5) [17]. For the pristine In_2O_3 sensor, oxygen molecules are adsorbed on the surface of gas-sensing materials when the sensor is exposed to an air environment. In this process, oxygen molecules capture the free electrons from the conduction band of In_2O_3 , leading to the formation of adsorbed oxygen species $(O_2^-, O^-, \text{ or } O^2^-)$. Thus, a depletion layer is formed and the resistance of the sensor increases (Equations (2) and (3)). Once the reducing gas (HCHO) is introduced, the HCHO gas molecules react with adsorbed oxygen (Equation (4)), leading to the release of the electrons back into the conduction of In_2O_3 and resistance decreases. Gas sensing reactions are displayed as Equations (2)–(4):

$$O_2 \text{ (gas)} \rightarrow O_2 \text{ (ads)}$$
 (2)

$$O_2 \text{ (ads)} + e^- \rightarrow 2O^- \text{ (ads)} (100-400 \,^{\circ}\text{C})$$
 (3)

$$HCHO (gas) + 2O^{-} (ads) \rightarrow CO_{2} (gas) + H_{2}O (gas) + 2e^{-}$$
 (4)

The sensitization mechanisms of Pt/ZIF-8-derived Pt/ZnO-In $_2$ O $_3$ HNFs are displayed in Figure 5a. The improved HCHO sensing performance of 25PtZI sensor can be explained from the following aspects:

- (i) The heterojunctions between Pt, ZnO, and In_2O_3 , which is beneficial to facilitate the absorption of more oxygen molecules and target HCHO gases. Because In_2O_3 , Pt, and ZnO have different work functions, when they combine, electrons move from In_2O_3 to Pt and ZnO until their Fermi levels are the same, bending the energy bands at their interfaces (Figure 5a). This results in the formation of an electron depletion layer at the In_2O_3 interface and an electron accumulation layer at the ZnO interface, providing more active sites for gas sensing reactions. Furthermore, heterogeneous junctions have a greater ability to adsorb oxygen molecules and analyze gases [55]. This can be proved by XPS analysis, as the percentage of O_C in 25PtZI HNFs is 35.8%, higher than pristine In_2O_3 (30.0%). Since oxygen captures more electrons in the conduction band of In_2O_3 and ZnO, the electron thickness of these materials increases, along with the heterojunction potential between grains, which is why 25PtZI HNFs have a high resistance in air (Figure 4b). In an HCHO atmosphere, the HCHO molecules will react with abundant adsorbed oxygen (O^-) and more electrons are released into the conduction bands of In_2O_3 and Index I
- (ii) The optimal amount of Pt NPs catalysis is another major factor for the increased response value of the 25PtZI sensor. Uniformly loaded ultra-small Pt NPs on the surface of ZnO-In $_2$ O $_3$ can facilitate the dissociation of O $_2$ molecular into adsorbed oxygen (O $^-$) through the "spillover effect", increasing the concentration of adsorbed oxygen. In addition, as shown by XPS results, Pt has an oxidation state (PtO $_2$), resulting in a p-n heterojunction between p-type PtO $_2$ and n-type In $_2$ O $_3$ (ZnO), which increases the sensor resistance and

adds to the barrier height. Compared to the pristine In_2O_3 , 05PtZI, and 10PtZI sensors, the higher R_a value for the 25PtZI sensor indicates that there is more electron transfer on the interface (Figure 4b and Figure S2). And the higher R_a value facilitates a higher response of an n-type In_2O_3 sensor due to that the response is defined as R_a/R_g [56]. However, when the Pt content reached 0.5 wt%, the continuous nanofiber morphology of 50PtZI was slightly disrupted and the Pt particles agglomeration (Figure 2e), which led to the number of active sites reduced and the sensitivity of the 50PtZI sensor toward HCHO decreased [50].

(iii) Benefiting from the porous and framework structure of ZIF-8, the Pt/ZIF-8-derived 25PtZI HNFs possess a porous and hollow one-dimensional nanofiber morphology, which can effectively promote gas adsorption and diffusion through the inner and outer surfaces of the entire structure, thereby accelerating the response and recovery speed of the gas sensor [4].

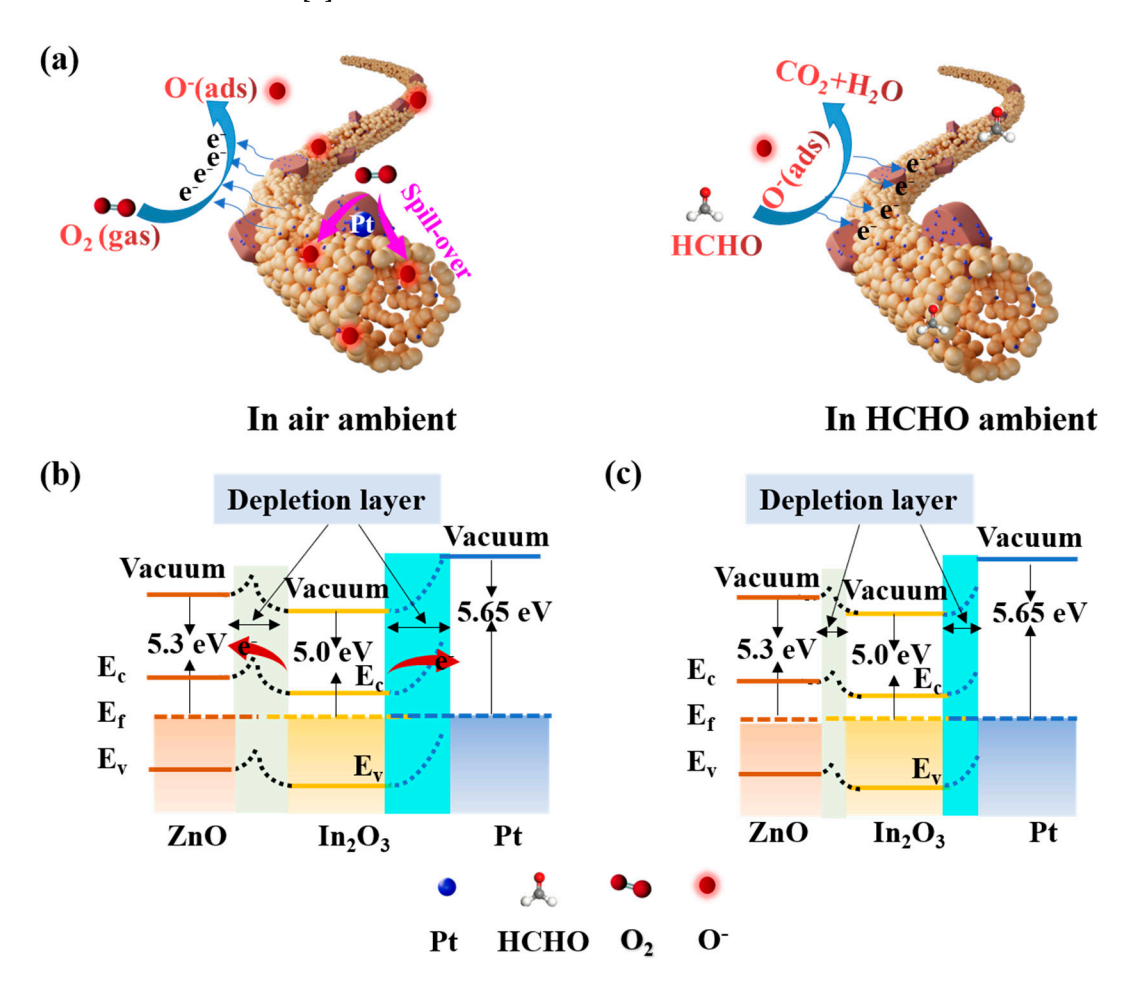


Figure 5. (a) Schematic illustrations of HCHO gas sensing mechanism of sensor based on 25PtZI HNFs. (b,c) Corresponding energy band diagrams in air and in HCHO.

4. Conclusions

In conclusion, the Pt/ZIF-8-derived porous Pt/ZnO-In $_2$ O $_3$ electrospun hollow nanofibers were developed by a simple electrospinning method via dispersing Pt in ZIF-8 nanocages as a sacrificial template. Nanofibers could effectively be incorporated with ultra-small Pt nanoparticles using this method. Five control samples of pristine In $_2$ O $_3$, 05PtZI, 10PtZI, 25PtZI, and 50PtZI HNFs were prepared by modulating the addition of Pt. The response value of the 25PtZI sensor was 48.3 toward 100 ppm HCHO at 180 °C, which was the highest among all the other sensors. In addition, the 25PtZI sensor possessed a rapid response and recovery speed (5/22 s) and outstanding long-term stability. Its theoretical

LODs could be as low as 74.6 ppb. The superior sensing performance of 25PtZI sensor is due to the synergistic effect of the heterojunctions formed between Pt, ZnO, and $\rm In_2O_3$ components, coupled with the catalytic effect of ultra-small Pt NPs derived from Pt/ZIF-8. This work offers an innovative approach that involves utilizing MOFs as a support for the acquisition of ultra-small noble metal catalysts, thereby achieving highly sensitive HCHO gas sensors.

Supplementary Materials: The following supporting information can be downloaded at: https://www.mdpi.com/article/10.3390/chemosensors12060093/s1, Figure S1: EDS spectra for (a) In₂O₃, (b) 05PtZI, (c) 10PtZI, (d) 25PtZI, and (e) 50PtZI HNFs, Figure S2: Base resistance in air of all sensors under different operating temperatures, Figure S3: Response–recovery curves of four sensors toward 100 ppm HCHO, Figure S4: Repeatability of the 25PtZI sensor to HCHO (100 ppm) at 220 °C, Figure S5: TGA curve of the 25PtZI HNFs, Table S1: ICP-AES analysis for 05PtZI, 10PtZI, 25PtZI, and 50PtZI, Table S2: The relative percentages of three different oxygen species for pristine In₂O₃ and 25PtZI HNFs, Table S3: Comparison of HCHO gas sensing performance with other gas sensors [57–61].

Author Contributions: Conceptualization, L.Z., Z.W., and W.Y.; methodology, L.Z. and Z.W.; validation, L.Z., Z.W., J.L., and W.Y.; formal analysis, L.Z., J.W., and J.Z.; investigation, L.Z. and J.Z.; resources, J.L. and W.Y.; data curation, Z.W. and J.Z.; writing—original draft preparation, L.Z. and Z.W.; writing—review and editing, L.Z., J.W., and W.Y.; visualization, L.Z. and J.L.; supervision, L.Z., J.W., and W.Y.; funding acquisition, L.Z., J.L., and W.Y. All authors have read and agreed to the published version of the manuscript.

Funding: This research was funded by the National Natural Science Foundation of China (51978569, and 52302198), the Natural Science Foundation of Shaanxi Province (2023-JC-QN-0494), the Young Talent Research Project of Shaanxi Science and Technology Association (20220401), the China Post-doctoral Science Foundation (2023M742788), the Scientific Research Program Funded by Shaanxi Provincial Education Department (No. 23JK0445), and the Shaanxi Province Postdoctoral Science Foundation (2023BSHEDZZ30).

Institutional Review Board Statement: Not applicable.

Informed Consent Statement: Not applicable.

Data Availability Statement: The data that have been used are confidential.

Conflicts of Interest: The authors declare no conflicts of interest.

References

 Zhang, Y.; Wang, M.; San, X.; Zhang, L.; Wang, N.; Wang, G.; Meng, D.; Shen, Y. Highly selective gas sensors for formaldehyde detection based on ZnO@ZIF-8 core-shell heterostructures. Sens. Actuators B 2024, 398, 134689. [CrossRef]

- 2. Souri, M.; Salar Amoli, H.; Yamini, Y. Three-dimensionally ordered porous In-doped SmFeO₃ perovskite gas sensor for highly sensitive and selective detection of formaldehyde. *Sens. Actuators B* **2024**, *404*, 135213. [CrossRef]
- 3. Min, Y.; Yuan, C.; Fu, D.; Liu, J. Formaldehyde Gas Sensors Fabricated with Polymer-Based Materials: A Review. *Chemosensors* **2023**, *11*, 134. [CrossRef]
- 4. Zhang, Y.; Xu, D.; Zhou, T.; Song, Z.; Deng, Z.; Zi, B.; Zhang, J.; Zhao, J.; Liu, Q.; Hu, G. Nonstoichiometric Doping of $La_{0.9}Fe_xSn_{1-x}O_3$ Hollow Microspheres for an Ultrasensitive Formaldehyde Sensor. *ACS Sens.* **2023**, 8, 4334–4343. [CrossRef] [PubMed]
- 5. Park, J.; Lee, J.; Choi, M.S.; Huh, J.-S. Formaldehyde Gas Sensing Characteristics of ZnO-TiO₂ Gas Sensors. *Chemosensors* **2023**, 11, 140. [CrossRef]
- 6. Zhou, L.; Chang, X.; Zheng, W.; Liu, X.; Zhang, J. Single atom Rh-sensitized SnO₂ via atomic layer deposition for efficient formaldehyde detection. *Chem. Eng. J.* **2023**, 475, 146300. [CrossRef]
- 7. Zhang, H.; Guo, S.; Zheng, W.; Wang, H.; Li, H.-Y.; Yu, M.-H.; Chang, Z.; Bu, X.-H.; Liu, H. Facile engineering of metal–organic framework derived SnO₂-ZnO composite based gas sensor toward superior acetone sensing performance. *Chem. Eng. J.* **2023**, 469, 143927. [CrossRef]
- 8. Liu, L.; Zhou, P.; Su, X.; Liu, Y.; Sun, Y.; Yang, H.; Fu, H.; Qu, X.; Liu, S.; Zheng, S. Synergistic Ni single atoms and oxygen vacancies on SnO₂ nanorods toward promoting SO₂ gas sensing. *Sens. Actuators B* **2022**, *351*, 130983. [CrossRef]

9. Huang, D.; Yong, P.; Shen, S. MOF-decorated sea urchin-like In₂O₃ gas sensor with higher gas sensitivity to formaldehyde. *J. Solid State Chem.* **2023**, 328, 124336. [CrossRef]

- 10. Ou, Y.; Zhu, G.; Liu, P.; Jia, Y.; Zhu, L.; Nie, J.; Zhang, S.; Zhang, W.; Gao, J.; Lu, H.; et al. Anchoring Platinum Clusters onto Oxygen Vacancy-Modified In₂O₃ for Ultraefficient, Low-Temperature, Highly Sensitive, and Stable Detection of Formaldehyde. *ACS Sens* **2022**, *7*, 1201–1212. [CrossRef] [PubMed]
- 11. Chen, X.; Liu, T.; Han, L.; Yin, X.-T. High-response of NiO-modified self-assembled nanosheets formed with ZnO nanoparticles for n-butanol detection. *Sens. Actuators B* **2023**, *390*, 134011. [CrossRef]
- 12. Yuan, Z.; Li, J.; Meng, F. High response n-propanol sensor based on co-modified ZnO nanorods. *J. Alloys Compd.* **2022**, 910, 164971. [CrossRef]
- 13. Thamaga, B.R.J.; Theka, T.J.; Motsoeneng, R.G.; Coetsee-Hugo, L.; Swart, H.C.; Motaung, D.E. Remarkable surface area engineering of nanosheet-assembled hierarchical p-n Ag-loaded NiO-CeO₂ heterostructure for superior ethanol sensing performance. *J. Alloys Compd.* **2024**, 976, 173110. [CrossRef]
- 14. Shi, C.; Yu, L.; He, X.; Zhang, Y.; Liu, J.; Li, S.; Zhang, C.; Cao, L.; Nan, N.; Du, H.; et al. Vertically aligned mesoporous Ce doped NiO nanowalls with multilevel gas channels for high-performance acetone gas sensors. *Sens. Actuators B* **2024**, 401, 134888. [CrossRef]
- 15. Meng, D.; Xie, Z.; Wang, M.; Xu, J.; San, X.; Qi, J.; Zhang, Y.; Wang, G.; Jin, Q. In Situ Fabrication of SnS₂/SnO₂ Heterostructures for Boosting Formaldehyde—Sensing Properties at Room Temperature. *Nanomaterials* **2023**, *13*, 2493. [CrossRef] [PubMed]
- 16. Ghasemi, F.; Ghasemi, M.; Eftekhari, L.; Soleimanian, V. Comparison and influence of metal dopants on the opto-electrical, microstructure and gas sensing properties of nanostructured indium oxide films. *Opt. Laser Technol.* **2022**, *146*, 107564. [CrossRef]
- Liu, N.; Li, Y.; Li, Y.; Cao, L.; Nan, N.; Li, C.; Yu, L. Tunable NH₄F-Assisted Synthesis of 3D Porous In₂O₃ Microcubes for Outstanding NO₂ Gas-Sensing Performance: Fast Equilibrium at High Temperature and Resistant to Humidity at Room Temperature. ACS Appl. Mater. Interfaces 2021, 13, 14355–14364. [CrossRef] [PubMed]
- 18. Bu, W.; Zhang, Y.; Qin, Q.; Li, Y.; Chuai, X.; Zhou, Z.; Hu, C.; Wang, T.; Sun, P.; Liu, F.; et al. Improved ppb-level NO₂ conductometric sensor induced by trace Au on SnO₂ nanosheet. *Sens. Actuators B* **2023**, *379*, 133237. [CrossRef]
- 19. Li, C.; Zheng, F.; Mi, X.; Wei, B.; Zhang, X. Pd-based eye-readable H₂ sensors: Principles, developments, and perspectives. *Opt. Laser Technol.* **2024**, *176*, 110955. [CrossRef]
- 20. Xiao, Y.; Hu, S.; Liu, Y.; Zhang, A.; Yao, Z.; Tian, Y.; Li, H.; Ning, Y.; Li, F.; Qu, F.; et al. Pt-modified BiVO₄ nanosheets for enhanced acetone sensing. *Sens. Actuators B* **2023**, *389*, 133853. [CrossRef]
- 21. Zhao, Y.; Wang, S.; Yuan, W.; Fan, S.; Hua, Z.; Wu, Y.; Tian, X. Selective detection of methane by Pd-In₂O₃ sensors with a catalyst filter film. *Sens. Actuators B* **2021**, *328*, 129030. [CrossRef]
- 22. Liu, D.; Pan, J.; Tang, J.; Liu, W.; Bai, S.; Luo, R. Ag decorated SnO₂ nanoparticles to enhance formaldehyde sensing properties. *J. Phys. Chem. Solids* **2019**, 124, 36–43. [CrossRef]
- 23. Sui, N.; Xu, Y.; Zhang, P.; Cao, S.; Zhou, T.; Zhang, T. MIL-68 (In) and ZIF-8 assisted construction of n-n heterostructure for the effective sensing of trace-level ozone. *Sens. Actuators B* **2023**, *380*, 133312. [CrossRef]
- 24. Fan, X.; Yang, S.; Huang, C.; Lu, Y.; Dai, P. Preparation and Enhanced Acetone-Sensing Properties of ZIF-8-Derived Co₃O₄@ZnO Microspheres. *Chemosensors* **2023**, *11*, 376. [CrossRef]
- 25. Zhang, J.; Lu, H.; Zhang, L.; Leng, D.; Zhang, Y.; Wang, W.; Gao, Y.; Lu, H.; Gao, J.; Zhu, G.; et al. Metal–organic framework-derived ZnO hollow nanocages functionalized with nanoscale Ag catalysts for enhanced ethanol sensing properties. *Sens. Actuators B* **2019**, 291, 458–469. [CrossRef]
- Qin, Y.; Xie, J.; Liu, S.; Bai, Y. Selective methanol-sensing of SnS-supported ultrathin ZIF-8 nanocomposite with core-shell heterostructure. Sens. Actuators B 2022, 368, 132230. [CrossRef]
- 27. Guo, S.; Wang, J.; Chen, F.; Sun, Y.; Liu, Y.; Wang, L.; Li, C. String of ZIF-derived hollow beaded nanocage embedded into carbon nanofiber with intensified exposed Co-Nx sites for efficient oxygen catalysis in various fuel cell devices. *Chem. Eng. J.* 2023, 463, 142498. [CrossRef]
- 28. Hung, C.M.; Phuong, H.V.; Van Thinh, V.; Hong, L.T.; Thang, N.T.; Hanh, N.H.; Dich, N.Q.; Van Duy, N.; Van Hieu, N.; Hoa, N.D. Au doped ZnO/SnO₂ composite nanofibers for enhanced H₂S gas sensing performance. *Sens. Actuators A Phys.* **2021**, 317, 112454. [CrossRef]
- 29. Wei, C.; Zhu, M.; Zhou, Z.; Zhao, S.; Mao, J.; Yin, D.; Li, J.; Wang, Y.; Hao, J. Two-dimensional Bi₂O₂S based high-sensitivity and rapid-response humidity sensor for respiratory monitoring and Human-Machine Interaction. *Chem. Eng. J.* **2024**, 485, 149805. [CrossRef]
- 30. Yang, Y.; Liu, C.; Wang, Y.; Hao, J. Nanorods Assembled Hierarchical Bi₂S₃ for Highly Sensitive Detection of Trace NO₂ at Room Temperature. *Chemosensors* **2024**, *12*, 8. [CrossRef]
- 31. Zhang, W.; Wang, X.; Wu, J.; Wang, X.; Lv, X.; Liu, G.; Li, B.; Zhou, J.; Xie, E.; Zhang, Z. Electrospun Nb-doped CeO₂ nanofibers for humidity independent acetone sensing. *Appl. Surf. Sci.* **2022**, *602*, 154303. [CrossRef]
- 32. Sun, Y.; Wang, B.; Wang, B.; Zhao, Z.; Zhang, W.; Zhang, W.; Suematsu, K.; Hu, J. Construction of Flower-like PtOx@ZnO/In₂O₃ Hollow Microspheres for Ultrasensitive and Rapid Trace Detection of Isopropanol. *ACS Appl. Mater. Interfaces* **2023**, 15, 12041–12051. [CrossRef] [PubMed]

33. Zhao, F.; Lu, Q.; Liu, S.; Wang, C. In₂O₃/ZnO heterostructured nanotubes: Electrospinning fabrication, characterization, and highly enhanced photocatalytic properties. *J. Sol-Gel Sci. Technol.* **2014**, 72, 137–143. [CrossRef]

- 34. Faisal, M.; Khan, S.B.; Rahman, M.M.; Jamal, A.; Asiri, A.M.; Abdullah, M.M. Synthesis, characterizations, photocatalytic and sensing studies of ZnO nanocapsules. *Appl. Surf. Sci.* 2011, 258, 672–677. [CrossRef]
- 35. Das, A.; Patra, M.; Bhagavathiachari, M.; Nair, R.G. Role of type II heterojunction in ZnO–In₂O₃ nanodiscs for enhanced visible-light photocatalysis through the synergy of effective charge carrier separation and charge transport. *Mater. Chem. Phys.* **2021**, 263, 124431. [CrossRef]
- 36. Rini, A.S.; Linda, T.M.; Hamzah, Y.; Umar, L.; Sari, M.; Rati, Y. Antibacterial activity of green synthesized ZnO nano-flower using pineapple peel extract. *Adv. Nat. Sci. Nanosci. Nanotechnol.* **2023**, *14*, 025008. [CrossRef]
- 37. Elouali, S.; Bloor, L.G.; Binions, R.; Parkin, I.P.; Carmalt, C.J.; Darr, J.A. Gas sensing with nano-indium oxides (In₂O₃) prepared via continuous hydrothermal flow synthesis. *Langmuir* **2012**, *28*, 1879–1885. [CrossRef] [PubMed]
- 38. Ziemba, M.; Schumacher, L.; Hess, C. Reduction behavior of cubic In₂O₃ nanoparticles by combined multiple in situ spectroscopy and DFT. *J. Phys. Chem. Lett.* **2021**, *12*, 3749–3754. [CrossRef] [PubMed]
- 39. Park, S.; Eom, T.-Y.; Jeong, R.-H.; Lee, H.-J.; Boo, J.-H. Synthesis and characterization of Al-doped ZnO/CdO heterostructured nanocomposites for enhancing NO₂ gas sensing performance. *Appl. Surf. Sci.* **2024**, *657*, 159746. [CrossRef]
- 40. Inyawilert, K.; Wisitsoraat, A.; Liewhiran, C.; Tuantranont, A.; Phanichphant, S. H₂ gas sensor based on PdOx-doped In₂O₃ nanoparticles synthesized by flame spray pyrolysis. *Appl. Surf. Sci.* **2019**, 475, 191–203. [CrossRef]
- 41. Li, L.; Zhou, L.; Hu, Z.; Li, T.; Chen, B.; Li, H.-Y.; Liu, H. Hollow-Out Fe₂O₃-Loaded NiO Heterojunction Nanorods Enable Real-Time Exhaled Ethanol Monitoring under High Humidity. *ACS Appl. Mater. Interfaces* **2023**, *15*, 15707–15720. [CrossRef] [PubMed]
- 42. Liu, W.; Xie, Y.; Chen, T.; Lu, Q.; Ur Rehman, S.; Zhu, L. Rationally designed mesoporous In₂O₃ nanofibers functionalized Pt catalysts for high-performance acetone gas sensors. *Sens. Actuators B* **2019**, 298, 126871. [CrossRef]
- 43. Zhou, Q.; Xu, L.; Kan, Z.; Yang, L.; Chang, Z.; Dong, B.; Bai, X.; Lu, G.; Song, H. A multi-platform sensor for selective and sensitive H₂S monitoring: Three-dimensional macroporous ZnO encapsulated by MOFs with small Pt nanoparticles. *J. Hazard. Mater.* **2022**, 426, 128075. [CrossRef] [PubMed]
- 44. Li, X.; He, W.; Li, C.; Song, B.; Liu, S. Synergetic surface modulation of ZnO/Pt@ZIF-8 hybrid nanorods for enhanced photocatalytic CO₂ valorization. *Appl. Catal. B* **2021**, 287, 119934. [CrossRef]
- 45. Guo, L.; Chen, F.; Xie, N.; Kou, X.; Wang, C.; Sun, Y.; Liu, F.; Liang, X.; Gao, Y.; Yan, X.; et al. Ultra-sensitive sensing platform based on Pt-ZnO-In₂O₃ nanofibers for detection of acetone. *Sens. Actuators B* **2018**, 272, 185–194. [CrossRef]
- 46. Sui, C.; Zhang, M.; Li, Y.; Wang, Y.; Liu, Y.; Liu, Z.; Bai, J.; Liu, F.; Lu, G. Pd@Pt Core–Shell Nanocrystal-Decorated ZnO Nanosheets for ppt-Level NO₂ Detection. *ACS Sens.* **2024**, *9*, 1967–1977. [CrossRef] [PubMed]
- 47. Yang, J.Q.; Han, W.J.; Ma, J.; Wang, C.; Shimanoe, K.; Zhang, S.M.; Sun, Y.F.; Cheng, P.F.; Wang, Y.L.; Zhang, H.; et al. Sn doping effect on NiO hollow nanofibers based gas sensors about the humidity dependence for triethylamine detection. *Sens. Actuators B* **2021**, *340*, 129971. [CrossRef]
- 48. Lou, C.; Yang, C.; Zheng, W.; Liu, X.; Zhang, J. Atomic layer deposition of ZnO on SnO₂ nanospheres for enhanced formaldehyde detection. *Sens. Actuators B* **2021**, 329, 129218. [CrossRef]
- 49. Zeb, S.; Peng, X.; Shi, Y.; Su, J.; Sun, J.; Zhang, M.; Sun, G.; Nie, Y.; Cui, Y.; Jiang, X. Bimetal Au-Pd decorated hierarchical WO₃ nanowire bundles for gas sensing application. *Sens. Actuators B* **2021**, 334, 129584. [CrossRef]
- 50. Luo, N.; Cai, H.; Lu, B.; Xue, Z.; Xu, J. Pt-functionalized Amorphous RuO(x) as Excellent Stability and High-activity Catalysts for Low Temperature MEMS Sensors. *Small* **2023**, *19*, e2300006. [CrossRef]
- 51. Wang, Q.; Li, R.; Wang, P.; Zhang, Y.; Wang, Y.; Yang, Y.; Wu, Z.; An, B.; Li, J.; Xie, E. Au-decorated WO₃-based sensor for chemiresistive detection of NO₂ at 80 °C. *Sens. Actuators B* **2023**, 390, 133985. [CrossRef]
- 52. Wang, Y.; Liu, Z.; Yang, L.; Li, Y.; Bai, J.; Sui, C.; Liu, Y.; Liang, X.; Liu, F.; Lu, G. Highly selective gas sensor for rapid detection of triethylamine using PdRu alloy nanoparticles functionalized SnO₂. Sens. Actuators B **2023**, 379, 133205. [CrossRef]
- 53. Wang, Y.; Zhou, Y. Recent Progress on Anti-Humidity Strategies of Chemiresistive Gas Sensors. *Materials* **2022**, *15*, 8728. [CrossRef] [PubMed]
- 54. Yang, K.; Ma, J.Z.; Qiao, X.K.; Cui, Y.W.; Jia, L.C.; Wang, H.Q. Hierarchical porous LaFeO₃ nanostructure for efficient trace detection of formaldehyde. *Sens. Actuators B* **2020**, *313*, 128022. [CrossRef]
- 55. Liu, J.; Zhang, L.; Cheng, B.; Fan, J.; Yu, J. A high-response formaldehyde sensor based on fibrous Ag-ZnO/In₂O₃ with multi-level heterojunctions. *J. Hazard. Mater.* **2021**, *413*, 125352. [CrossRef] [PubMed]
- 56. Ai, T.; Zhang, J.; Li, J.; Zhang, Y.; Yin, Y.; Lu, J. Ultrafast response of Pt functionalized Fe₂(MoO₄)₃ nanoflower gas sensors for ultra-low ppm level H₂ gas detection. *J. Alloys Compd.* **2024**, 970, 172567. [CrossRef]
- 57. Lou, C.; Huang, Q.; Li, Z.; Lei, G.; Liu, X.; Zhang, J. Fe₂O₃-sensitized SnO₂ nanosheets via atomic layer deposition for sensitive formaldehyde detection. *Sens. Actuators B* **2021**, 345, 130429. [CrossRef]
- 58. Cao, J.; Zhang, N.R.; Wang, S.M.; Zhang, H.M. Electronic structure-dependent formaldehyde gas sensing performance of the In₂O₃/Co₃O₄ core/shell hierarchical heterostructure sensors. *J. Colloid Interface Sci.* **2020**, 577, 19–28. [CrossRef] [PubMed]
- 59. Zhang, S.; Song, P.; Li, J.; Zhang, J.; Yang, Z.; Wang, Q. Facile approach to prepare hierarchical Au-loaded In₂O₃ porous nanocubes and their enhanced sensing performance towards formaldehyde. *Sens. Actuators B* **2017**, 241, 1130–1138. [CrossRef]

60. Li, Y.; Chen, N.; Deng, D.; Xing, X.; Xiao, X.; Wang, Y. Formaldehyde detection: SnO₂ microspheres for formaldehyde gas sensor with high sensitivity, fast response/recovery and good selectivity. *Sens. Actuators B* **2017**, 238, 264–273. [CrossRef]

61. Wang, X.S.; Zhang, J.B.; Wang, L.Y.; Li, S.C.; Liu, L.; Su, C.; Liu, L.L. High response gas sensors for formaldehyde based on Er-doped In₂O₃ nanotubes. *J. Mater. Sci. Technol.* **2015**, *31*, 1175–1180. [CrossRef]

Disclaimer/Publisher's Note: The statements, opinions and data contained in all publications are solely those of the individual author(s) and contributor(s) and not of MDPI and/or the editor(s). MDPI and/or the editor(s) disclaim responsibility for any injury to people or property resulting from any ideas, methods, instructions or products referred to in the content.